Supporting Information

Unveiling structural forms of Ru in WO_x-template catalysts for efficient acidic PEM water electrolysis

Xiongfeng Zeng,[1,2,3] Ao Cai,[1,2,3] Junhui Pei,[1,2] GuiXin Liu,[1,2] WenLu Li, [1,2] Xiaoman Xiong,[1,2***] Ding Zhou,[1,2**] Na Yao[1,2*]

[1] State Key Laboratory of New Textile Materials and Advanced Processing , Wuhan Textile University, Wuhan, Hubei 430073, P. R. China.

[2] Present address: No. 1 Sunshine Avenue, Jiangxia District, Wuhan, China,

[3] These authors contributed equally

*e-mail: yaona@wtu.edu.cn; Dingzhou@whu.edu.cn; 2023021@wtu.edu.cn

Experimental Section

Chemicals.

All chemicals were of analytical reagent grade and used as received without further purification. Tungstic acid (H_2WO_4; 99 %) were obtained from Shanghai Aladdin Biochemical Technology Co., Ltd and ruthenium chloride ($RuCl_3$; 97 %) were obtained from Shanghai Bide Pharmaceutical Technology Co., Ltd. Commercial 20 wt.% Pt/C, commercial RuO_2 and Nafion perfluorinated resin solution (5 wt.%) were purchased from Sigma-Aldrich. The Nafion 117 membranes were purchased from Zhengzhou YaoLe Instrument Technology Co., Ltd.

Materials Synthesis

Synthesis method of WO_3 powder: A certain amount of H_2WO_4 is transferred to a tube furnace, calcined at 600°C for 2 hours at a heating rate of 5°C/min, and taken out after cooling to room temperature to obtain WO_3 powder.

A typical synthesis protocol for the Ru_{SNCs}-WO_x catalyst entails the mixing of 100 mg of WO_3 powder and 50 mg of $RuCl_3$ in 15 mL of deionized water, subsequently followed by magnetic stirring for 30 minutes. The resultant mixture was then transferred into a 20 mL Teflon-lined autoclave. The mixture was maintained at 90 °C for a duration of 12 hours and thereafter permitted to cool down naturally to room temperature. The as-obtained powder was subjected to repeated washing with deionized water; subsequent to drying, it was transferred to a tubular furnace for calcination under an air atmosphere at 350 °C, with a heating ramp rate of 5 °C min^{-1} and a holding time of 2 hours. After cooling to room temperature, the product was subjected to filtration and subsequent drying to afford the Ru_{SNCs}-WO_x powder.

The Ru_{SAs}-WO_x catalyst was synthesized as follows: First, 10 mg of $RuCl_3$ was dissolved in 20 ml of water, 100 mg of WO_3 powder was added, and the mixture was impregnated overnight. The mixture was then dried and placed in a quartz boat. The boat was then transferred to a plasma-enhanced chemical vapor deposition (PECVD) instrument. The PECVD parameters were set as follows: temperature 400°C, radio frequency (RF) power 500 W, treatment time 40 minutes, tube pressure 50 Pa, and nitrogen flow. Finally, the instrument was started, and when the temperature reached the set value, the plasma generator was turned on. After the time expired, the plasma generator was turned off, and the instrument temperature was allowed to cool to room temperature to yield Ru_{SAs}-WO_x.

A typical synthesis method for the RuO_x/WO_x catalyst is to mix 40 mg of H_2WO_4 and 20 mg of $RuCl_3$ in 10 ml of water and stir for 2 hours. The powder is then transferred to a tube furnace and calcined at 450°C for 2 hours at a heating rate of 5°C/min. After cooling to room temperature, the RuO_x/WO_x catalyst is removed.

Material characterization

X-ray diffraction (XRD) patterns were collected on an Empyrean PANalytical diffractometer using Cu-Kα irradiation (40 kV, 40 mA, $\lambda = 1.5418$ Å) at a scan rate of 5° min-1. X-ray photoelectron spectroscopy (XPS) information was collected on a Thermo Fisher Scientific-ESCALAB 250Xi instrument. The peak data were calibrated based on the C 1s peak at 284.8 eV. Ru K-edge XAFS analysis was performed on the BL14W beamline of the Shanghai Synchrotron Radiation Facility (SSRF) using a Si(111) crystal monochromator. Prior to beamline analysis, the sample was placed in an aluminum sample holder and sealed with a thin film of Kapton tape. XAFS spectra were recorded at room temperature using a Bruker 5040 four-channel silicon drift detector (SDD). Ru K-edge extended X-ray absorption fine structure (EXAFS) spectra were recorded in transmission mode. For certain samples, the line shape and peak position of the ruthenium K-edge XANES spectra show minimal changes between scans. XAFS spectra for these standard samples were recorded in transmission mode. Spectra were processed and analyzed using Athena software.

Electrochemical characterization

Electrochemical characterizations were performed at room temperature using a CHI 760E electrochemical workstation utilizing a three-electrode configuration. A total of 2 mg of the Ru_{SNCs}-WO_x electrocatalyst was homogeneously dispersed in 1 mL of 0.1 wt% Nafion® resin solution, followed by ultrasonic treatment for 30 minutes to ensure complete homogenization. Subsequently, 80 μL of the resulting Ru_{SNCs}-WO_x catalyst ink was uniformly deposited onto a 1 cm × 1 cm carbon cloth (CC) substrate. The Ru_{SNCs}-WO_x-loaded CC, a high-purity graphite rod, and a saturated calomel electrode (SCE, Hg/Hg_2Cl_2) were employed as the working electrode, counter electrode, and reference electrode, respectively. Linear Sweep Voltammetry (LSV) measurements were performed in a 0.5 mol L^{-1} aqueous H_2SO_4 electrolyte over a potential range of 1 V to 1.5 V (vs. SCE) at a sweep rate of 5 mV s^{-1}. All experimentally recorded potentials were calibrated to the reversible hydrogen electrode (RHE) using the following equation: E (vs. RHE) = E (vs. SCE) + 0.059 × pH + 0.242 V. Linear Sweep Voltammetry (LSV) measurements were performed in 0.5 M H_2SO_4 at a scan rate of 5 mV s^{-1}, with 85% iR compensation applied.

Electrochemical surface area (ECSA) is an important measure to determine the number of active sites. The ECSA of each sample can be evaluated from electrochemical double capacitance (C_{dl}) according to the following equation:

$$\mathrm{ECSA}=\frac{Cdl}{Cs}$$

Where C_s is the specific capacitance of the sample or the capacitance of an atomically smooth planar surface of the material per unit area under identical electrolyte conditions, C_{dl} in the Faradaic potential region is calculated by linear fitting. The Cs are usually found to be in the range of 0.02-0.06 mF cm^{-2} per cm^2, and it is assumed as 0.035 mF cm^{-2} per cm^2 in the calculations of ECSA.

Take the calculation process of the TOF value of Ru_{SNCs}-WO_x as an example, and the details are described below:

$$\mathrm{TOF}=\frac{Total\ hydrogen\ turnovers\ per\ geometric\ area}{Active\ sites\ per\ geometric\ area}$$

Operando DEMS Isotope Labeling Test

Operando DEMS experiments were conducted on a Linglu differential electrochemical mass spectrometer. The electrolyte consisted of 0.5 M H_2SO_4 saturated with N_2. O_2 produced by the OER was analyzed in real time by entering the mass spectrometer vacuum chamber. Isotope labeling was performed using a sulfuric acid solution prepared with $H_2{}^{18}O$ enriched to ~97 atom% ^{18}O. The labeling process consisted of two steps:

1) Multiple LSV reactions (1.1–1.8 V vs RHE) were performed in $H_2{}^{18}O$/0.5 M H_2SO_4 to partially replace the catalyst lattice oxygen ($^{16}O\_L$) with ^{18}O;

2) Transfer the ^{18}O-labeled working electrode to the $H_2{}^{16}O$/0.5 M H_2SO_4 electrolyte and run LSV again, with the anode gaseous products recorded in real time by mass spectrometry. Simultaneously monitor the m/z = 32, 34, and 36 signals during each cycle.

The $34O_2$ signal originates from two ^{16}O-^{18}O coupling pathways:

(1) Lattice residual $^{16}O\_L$ couples with ^{18}O adsorbed species in $H_2{}^{18}O$;

(2) Lattice O_L coupled with $H_2{}^{16}O$-derived O adsorbed species

Measurement of local pH on the catalyst surface

According to the literature, the potential of IrO_x electrode is sensitive to pH and can be used to monitor the variations in the pH on the working electrode surface. In this work, the pH values on the catalyst surfaces were measured by an IrO_x-modified RRDE technique, with a disc diameter of 5.61 mm and a ring inner and outer diameter of 6.25 mm and 7.92 mm, respectively. Specifically, IrO_x was firstelectrodeposited onto the ring electrode (RE) of the RRDE by cyclic voltammetry. First, 0.15 g $IrCl_4$ was dissolved in 100 mL ultrapure water and stirred for 30 min, followed by the addition of 0.65 mg oxalic acid dihydrate. After 10 min, 1 mg H_2O_2 (30%) was added and after 10 min of stirring, the pH was raised to 10.5 with K_2CO_3. Next, the solution was heated at 90 °C for 15 min and cooled to room temperature in an ice bath to speed up its development. After preparation, the solution was aged at room temperature for a minimum of two days. Last, the deposition of IrO_x on the Ring electrode was carried out by means of cyclic voltammetry, using 300 cycles between -0.4 V and 0.75 V (vs. SCE) at 0.5 V s^{-1}.

Then, the pH dependence of the open circuit potential (E_{ocp}) was measured with the IrO_x-deposited RE. A three-electrode cell was constructed of the RRDE, graphite rod and a saturated calomel electrode (SCE) as working, counter, and reference electrodes, respectively. Then, the pH dependence of the open circuit potential (E_{ocp}) in Ar-saturated electrolyte was measured with IrO_x RE (Figure S20). The relationship between *Eocp* and the pH value of the ring electrode (pH_{ring}) can be described by the following equation

$$pH_{ring} = a \times (E_{ocp} + b) \qquad (1)$$

where a and b were obtained by linear fitting of E_{ocp} against the pH values of the bulk seawater (Figure S21).

Next, the measurement of pH on the catalyst surface was performed under different applied potentials. Linear sweep voltammetry was performed on the Ru_{SNCs}-WO_x-loaded disk electrode (DE)，Ru_{SAs}-WO_x-loaded disk electrode (DE) and RuO_x/WO_x-loaded disk electrode (DE) in 0.5 M H_2SO_4 electrolytes, and meanwhile, open circuit potential was recorded on the IrO_x-deposited RE. The pH value of the IrO_x-deposited RE was evaluated from the Eocp using equation (1). The pH value of the catalyst-loaded DE can be deducted from the pH value of the IrO_x-deposited RE by the following equation:

$$c_{H+,Ring} - c_{OH-,Ring} = N_D \times (c_{H+,Disk} - c_{OH-,Disk}) + (1 - N_D) \times (c_{H+,Bulk} - c_{OH-,Bulk}) \quad (2)$$

where $c_{H+,Ring}$ and $c_{H+,Disk}$ are the concentrations of H^+ on the RE and DE, respectively,

$c_{OH\text{-},Ring}$ and $c_{OH\text{-},Disk}$ are the concentrations of OH^- on the RE and DE, respectively, $c_{H+,Bulk}$ and $c_{OH\text{-},Bulk}$ are the concentrations of H^+ and OH^- in the bulk electrolyte, respectively, and $N_D = 0.37$ is the collection efficiency of the RE.

PEM measurements

In the proton exchange membrane (PEM) electrolyzer characterization, a membrane electrode assembly (MEA) with an active geometric area of 1 cm × 1 cm was precisely constructed via hot-pressing of the respective catalysts. Commercial platinum-on-carbon (Pt/C, 40 wt%) was adopted as the cathode catalyst, whereas the Ru_{SNCs}-WO_x electrocatalyst served as the anode catalyst. The Ru_{SNCs}-WO_x electrocatalytic powder was homogeneously dispersed in a mixture of isopropanol, deionized water, and 5 wt% Nafion® resin ethanol solution to formulate a uniform catalyst ink. The mass loading of the Pt/C (40 wt%) cathode was precisely controlled at 1 mg cm^{-2}, whereas that of the Ru_{SNCs}-WO_x anode was rigorously set to 2 mg cm^{-2}. The Ru_{SNCs}-WO_x electrocatalyst and Pt/C were separately cast onto polytetrafluoroethylene (PTFE) membranes via a controlled deposition process. Nafion® 117 was utilized as the PEM and subjected to successive treatment with hydrogen peroxide (H_2O_2) and 0.5 M sulfuric acid (H_2SO_4) at 80 °C for 1 hour to achieve surface activation. The PEM exhibited a dimension of 2.6 cm × 2.6 cm and a thickness of 183 μm. Following this, the catalyst-loaded PTFE membranes were hot-pressed onto the preconditioned Nafion® 117 membrane at 120 °C under a pressure of 10 MPa for 5 minutes so as to construct the MEA. Thereafter, a PEM water electrolyzer (PEMWE) was assembled and subjected to electrochemical testing at 30 °C using 0.5 M H_2SO_4 as the electrolyte. The polarization curve of the PEMWE was recorded at a sweep rate of 5 mV s^{-1}, and a long-term chronopotentiometric measurement was performed at a constant current density of 1 A cm^{-2} to systematically evaluate its electrochemical stability over an extended period.

DFT calculations

DFT calculations were performed with VASP software using the Perdew–Burke–

Ernzerhof (PBE) energy level and projector augmented wave (PAW) methods. The PAW method was used to represent core-valence electron interactions. A 4×4×1 Monkhorst–Pack k-point grid was used for Brillouin zone integration. Valence electron states were expanded on a plane-wave basis set with an energy cutoff of 570 eV. A Gaussian dispersion of 0.05 eV was used during geometry optimization. The convergence criterion for iterations in the self-consistent field (SCF) was set to 10^{-6} eV, and the residual forces for the optimized atomic positions were less than 0.02 eV/Å.

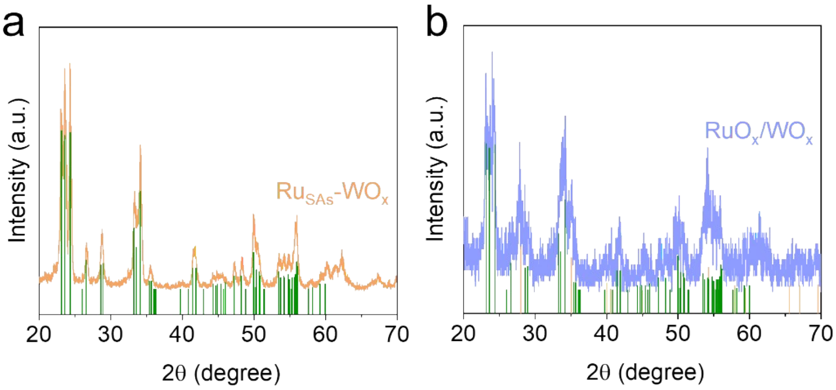

Fig. S1 XRD pattern of (a) Ru_{SAs}-WO_x; (b) RuO_x/WO_x.

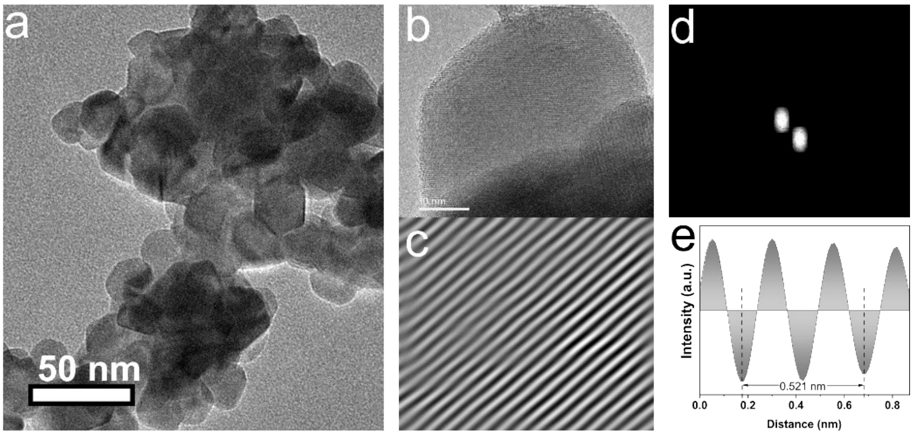

Fig. S2 TEM image of Ru_{SNCs}-WO_x.

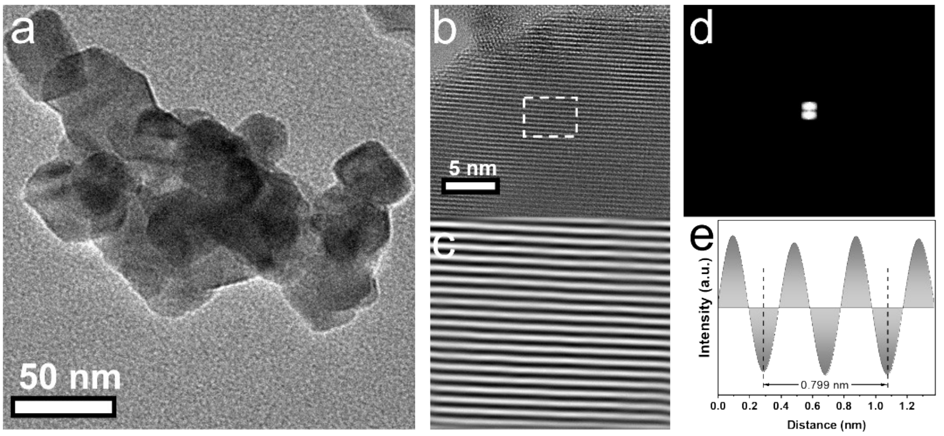

Fig. S3 TEM image of Ru_{SAs}-WO_x.

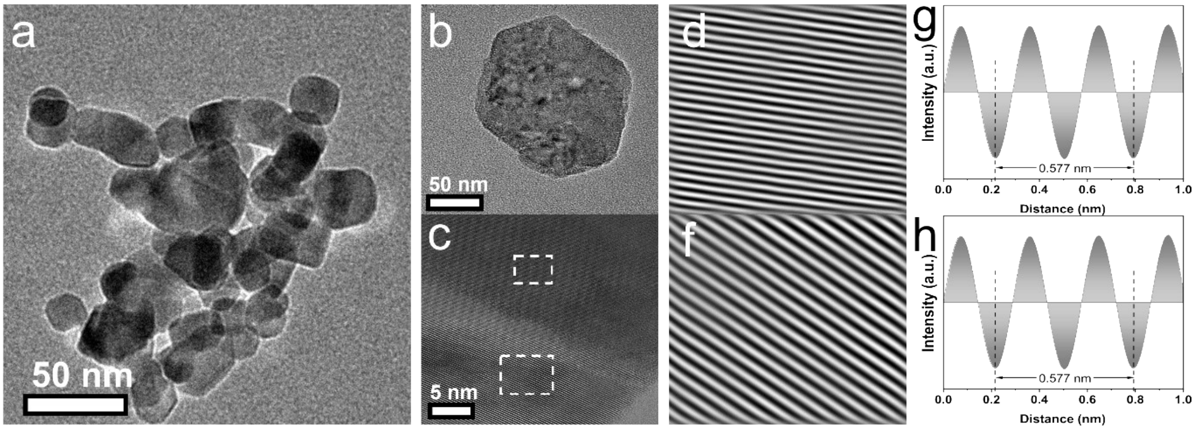

Fig. S4 TEM image of RuO_x/WO_x.

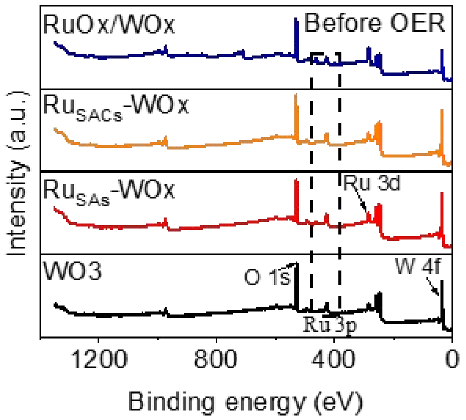

Fig. S5 XPS spectra of Ru_{SNCs}-WO_x, Ru_{SAs}-WO_x, and RuO_x/WO_x.

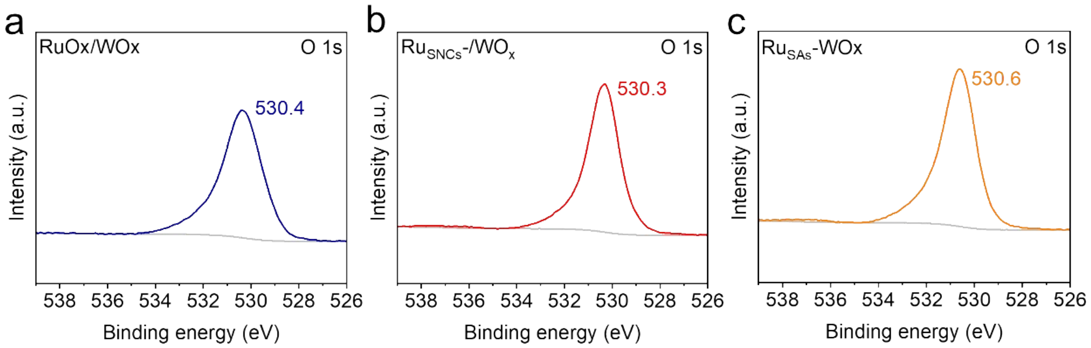

Fig. S6 XPS spectra of O 1*s* for (a) Ru_{SNCs}-WO_x; (b) Ru_{SAs}-WO_x; (c) RuO_x/WO_x.

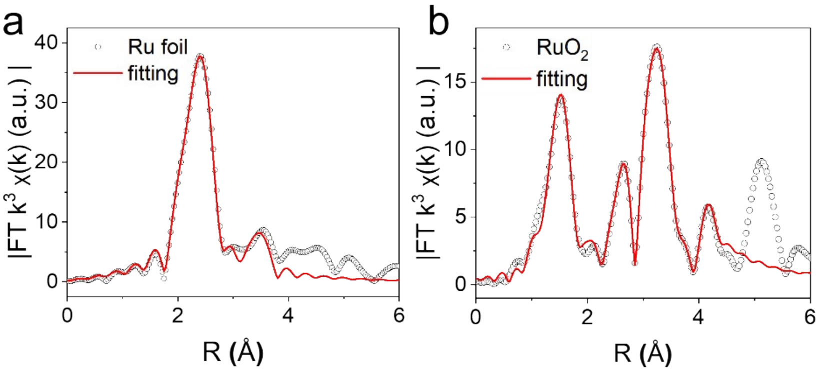

Fig. S7 Ru K-edge EXAFS fitting curves in R space for (a) Ru foil; (b) RuO_2.

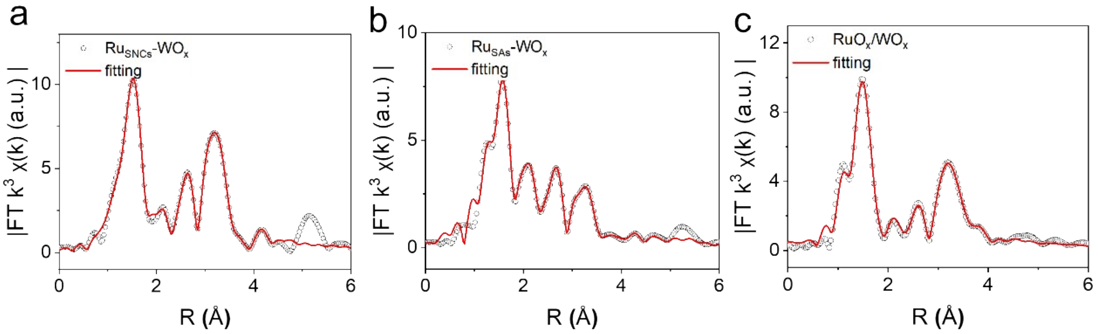

Fig. S8 Ru K-edge EXAFS fitting curves in R space for (a) Ru_{SNCs}-WO_x; (b) Ru_{SAs}-WO_x; (c) RuO_x/WO_x.

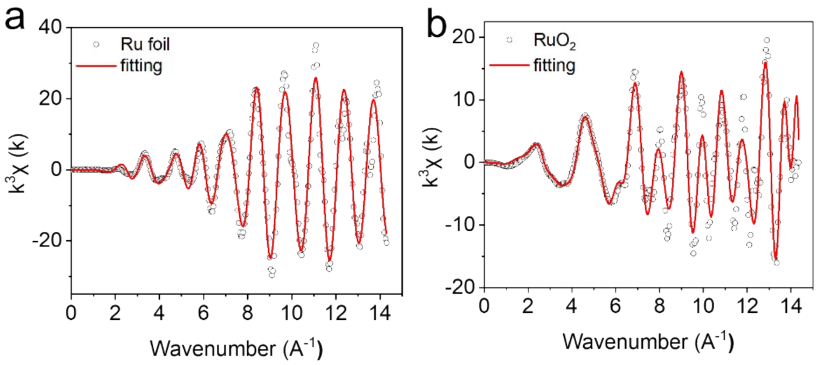

Fig. S9 Ru K-edge EXAFS fitting curves in k space for (a) Ru foil; (b) RuO$_2$.

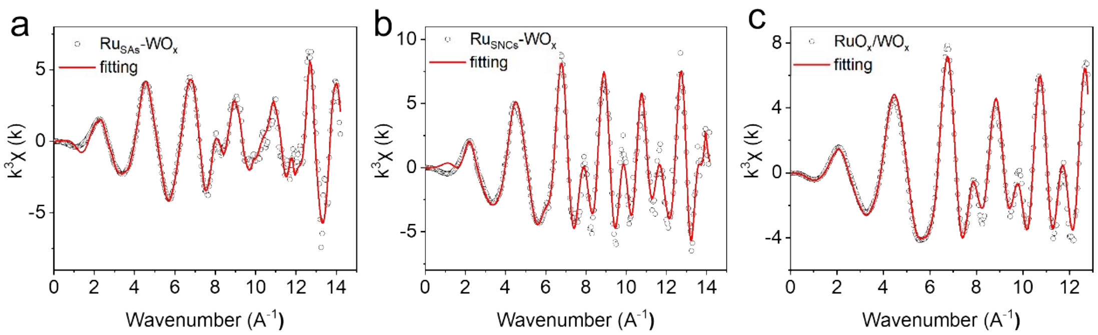

Fig. S10 Ru K-edge EXAFS fitting curves in k space for (a) Ru$_{SNCs}$-WO$_x$; (b) Ru$_{SAs}$-WO$_x$; (c) RuO$_x$/WO$_x$.

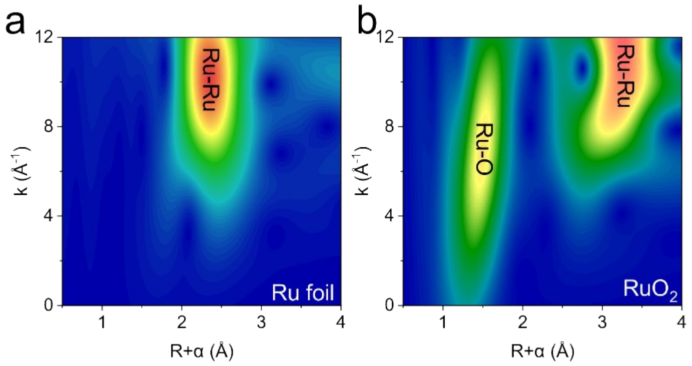

Fig. S11 Ru K-edge WT-EXAFS for (a) Ru foil; (b) RuO$_2$.

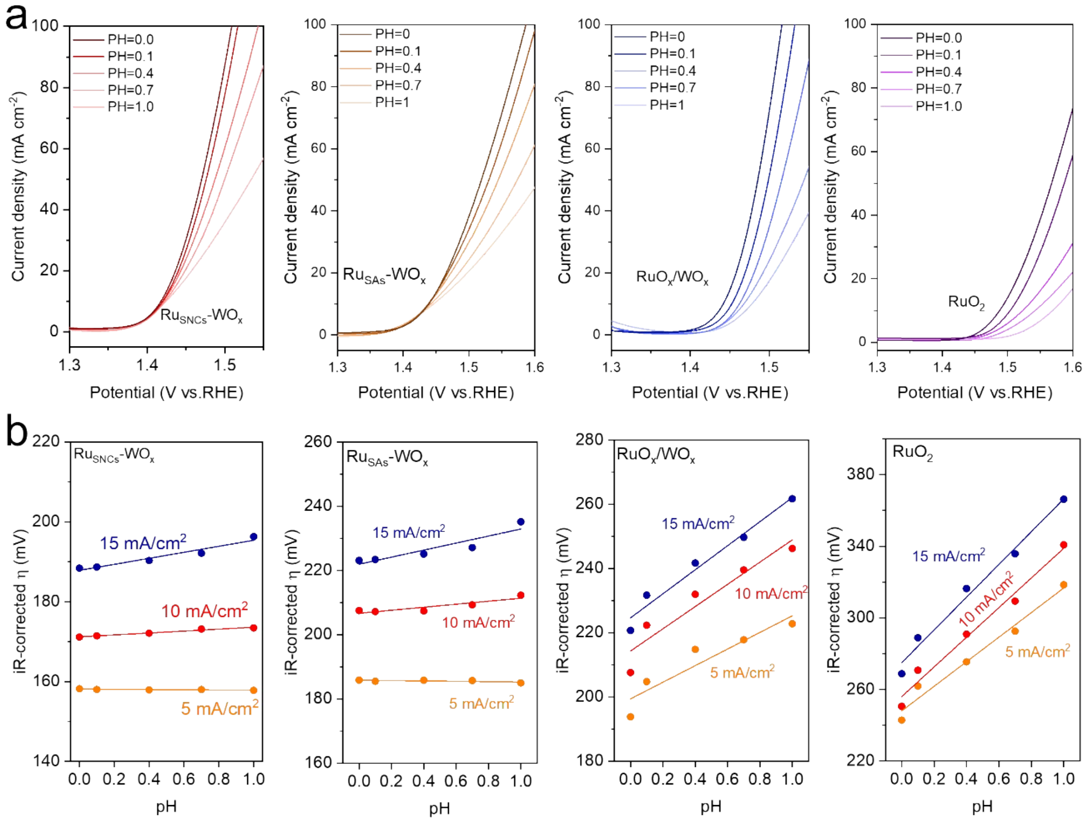

Fig. S12 pH independent OER activity of RuO$_2$, Ru$_{SNCs}$-WO$_x$, Ru$_{SAs}$-WO$_x$, and RuO$_x$/WO$_x$ on RHE scale. (a) OER activity of RuO$_2$, Ru$_{SNCs}$-WO$_x$, Ru$_{SAs}$-WO$_x$, and RuO$_x$/WO$_x$ with varying pH. (b) pH dependence on the OER potential at different current densities for RuO$_2$, Ru$_{SNCs}$-WO$_x$, Ru$_{SAs}$-WO$_x$, and RuO$_x$/WO$_x$.

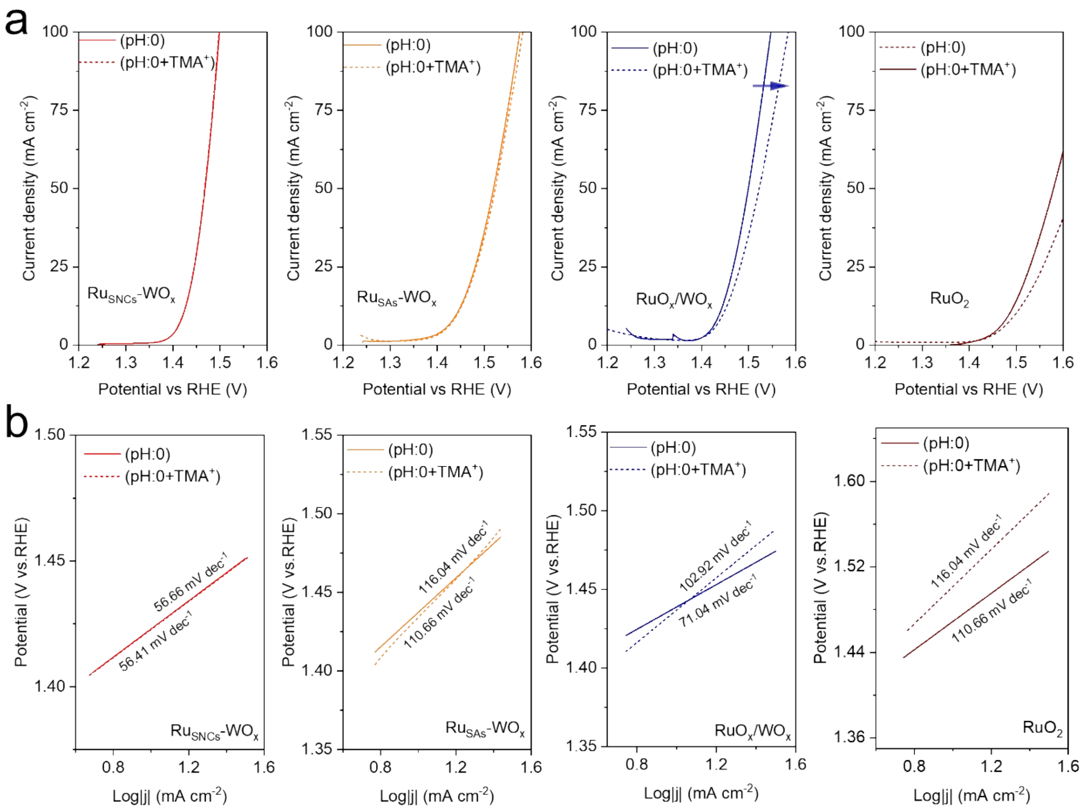

Fig. S13 (a) LSV curves of RuO_2, Ru_{SNCs}-WO_x, Ru_{SAs}-WO_x, and RuO_x/WO_x at different solutions (0.5M H_2SO_4 solutions, 0.5M H_2SO_4 solutions and 0.01M $TMANO_3$). (b) Tafel slopes plots RuO_2, Ru_{SNCs}-WO_x, Ru_{SAs}-WO_x, and RuO_x/WO_x at different solutions (0.5M H_2SO_4 solutions, 0.5M H_2SO_4 solutions and 0.01M $TMANO_3$).

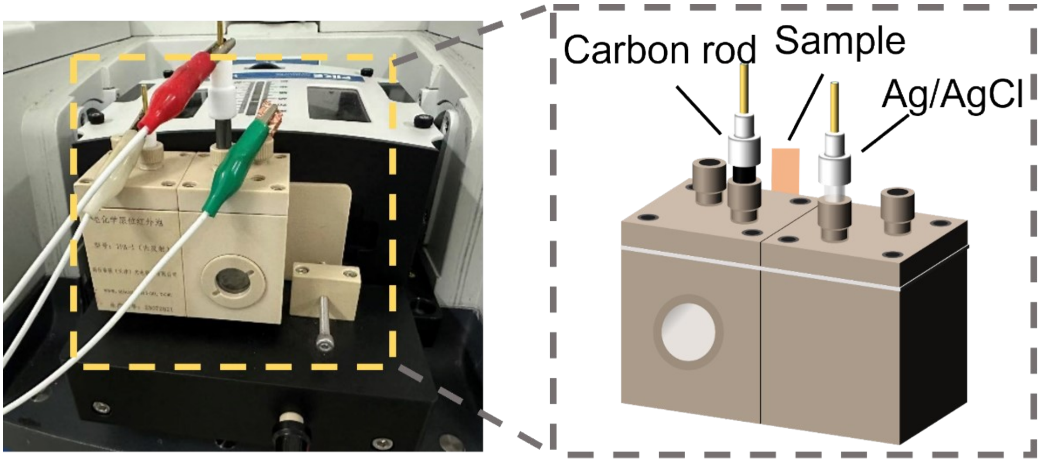

Fig. S14 In-situ FTIR device diagram.

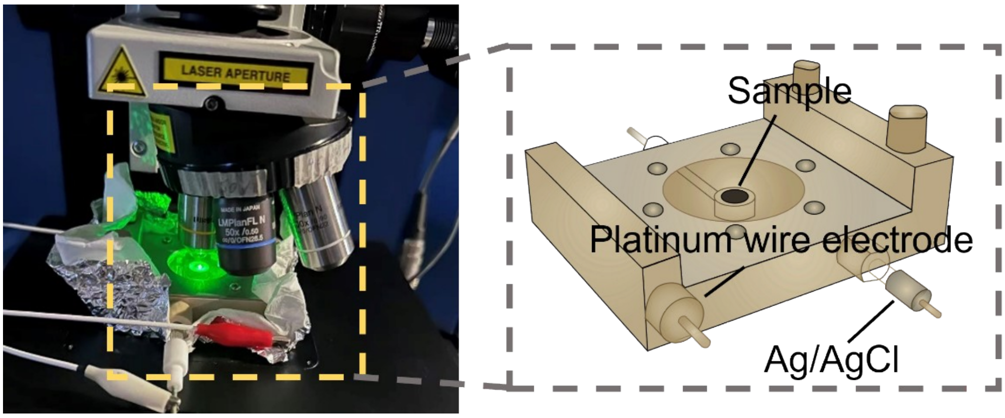

Fig. S15 In-situ Raman device diagram.

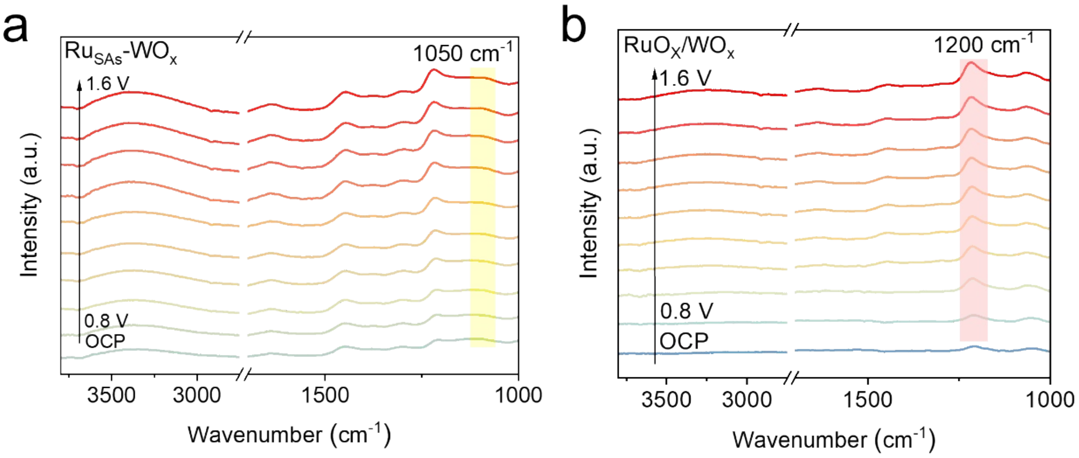

Fig. S16 In situ infrared spectra of Ru$_{SAs}$-WO$_x$ and RuO$_x$/WO$_x$.

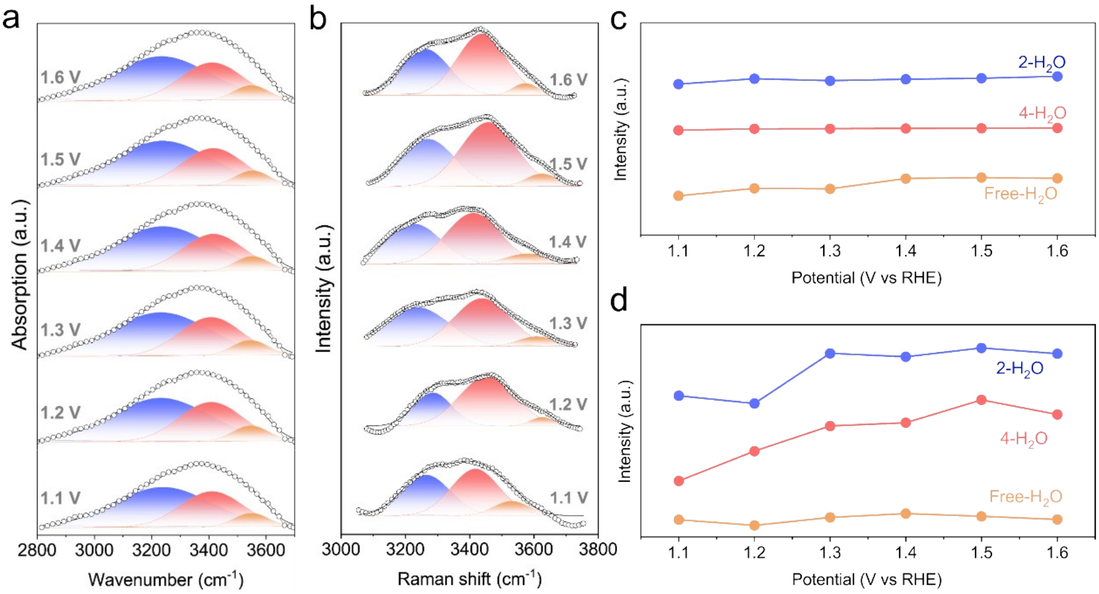

Fig. S17 (a) In situ FTIR spectra were recorded at potentials from OCV to 1.6 V on Ru$_{SAs}$-WO$_x$. (b) In situ Raman spectra were recorded at potentials from OCV to 1.6 V on Ru$_{SAs}$-WO$_x$. Percentage of different types of interfacial water structures at applied potential by (c) In situ FTIR spectra and (d) In situ Raman.

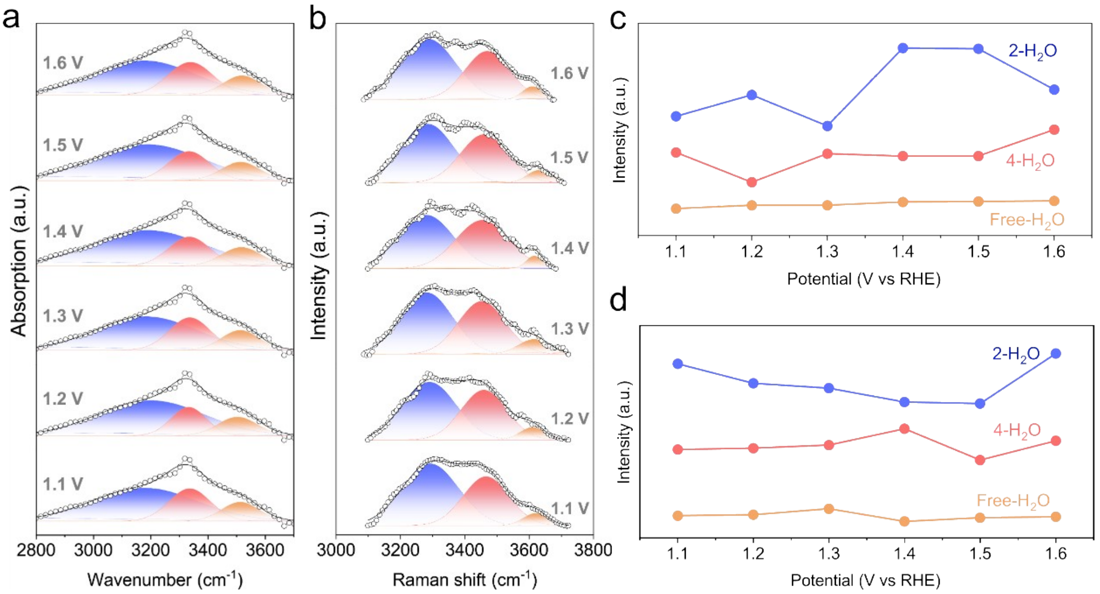

Fig. S18 (a) In situ FTIR spectra were recorded at potentials from OCV to 1.6 V on RuO_x/WO_x. (b) In situ Raman spectra were recorded at potentials from OCV to 1.6 V on RuO_x/WO_x . Percentage of different types of interfacial water structures at applied potential by (c) In situ FTIR spectra and (d) In situ Raman.

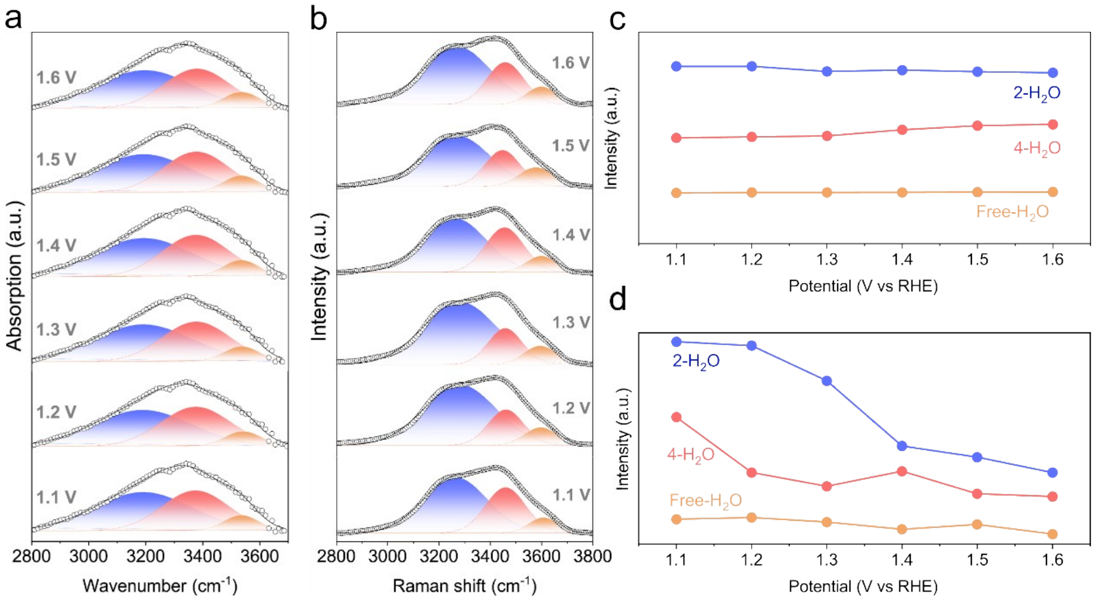

Fig. S19 (a) In situ FTIR spectra were recorded at potentials from OCV to 1.6 V on RuO_2. (b) In situ Raman spectra were recorded at potentials from OCV to 1.6 V on RuO_2 . Percentage of different types of interfacial water structures at applied potential by (c) In situ FTIR spectra and (d) In situ Raman.

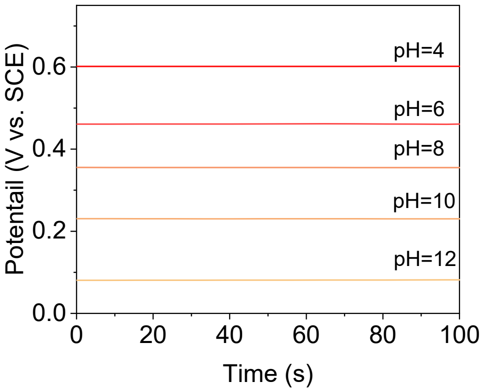

Fig. S20 Time dependence of OCP of the IrO_x electrodeposited electrode on different pH.

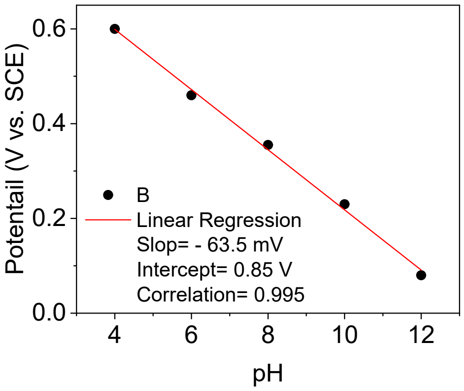

Fig. S21 pH dependence of OCP of IrO_x electrodeposited electrode.

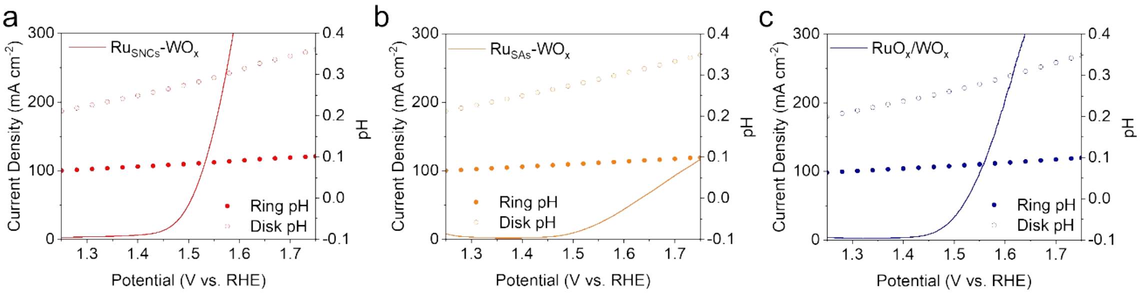

Fig. S22 OER polarization curves of (a) Ru_{SNCs}-WO_x; (b) Ru_{SAs}-WO_x and (c) RuO_x/WO_x and corresponding local pH under potential.

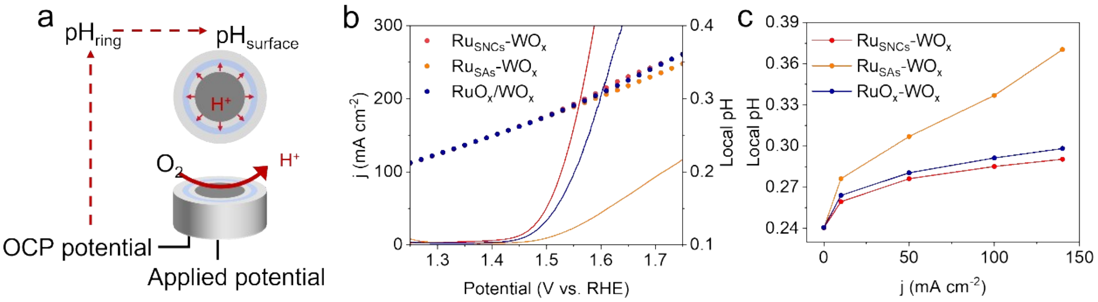

Fig. S23 (e) The schematic illustration of RRDE for monitoring local pH. (f) Changes of local pH on Ru_{SNCs}-WO_x Ru_{SAs}-WO_x and RuO_x/WO_x electrodes with the electrode potential. (g) Changes in local pH on Ru_{SNCs}-WO_x Ru_{SAs}-WO_x and RuO_x/WO_x

electrodes with the current densities.

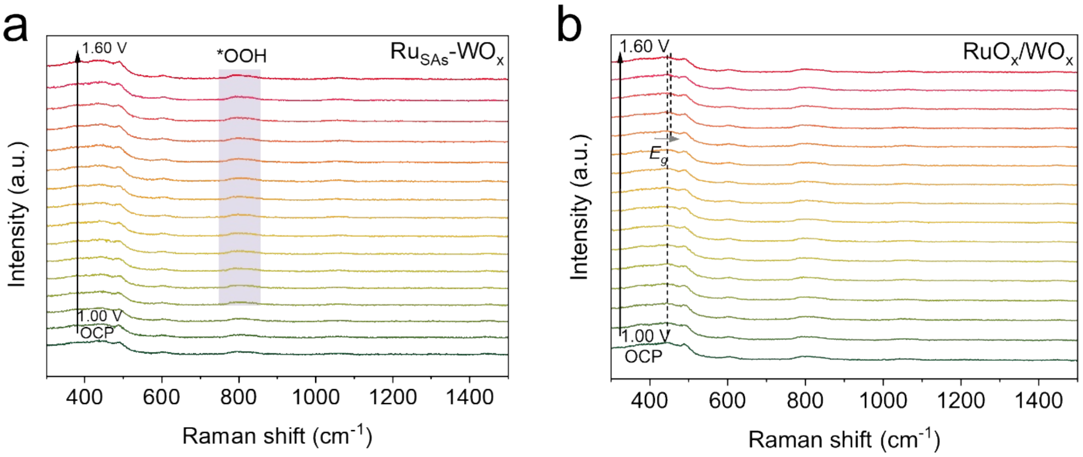

Fig. S24 In situ Raman spectra of Ru_{SAs}-WO_x and RuO_x/WO_x.

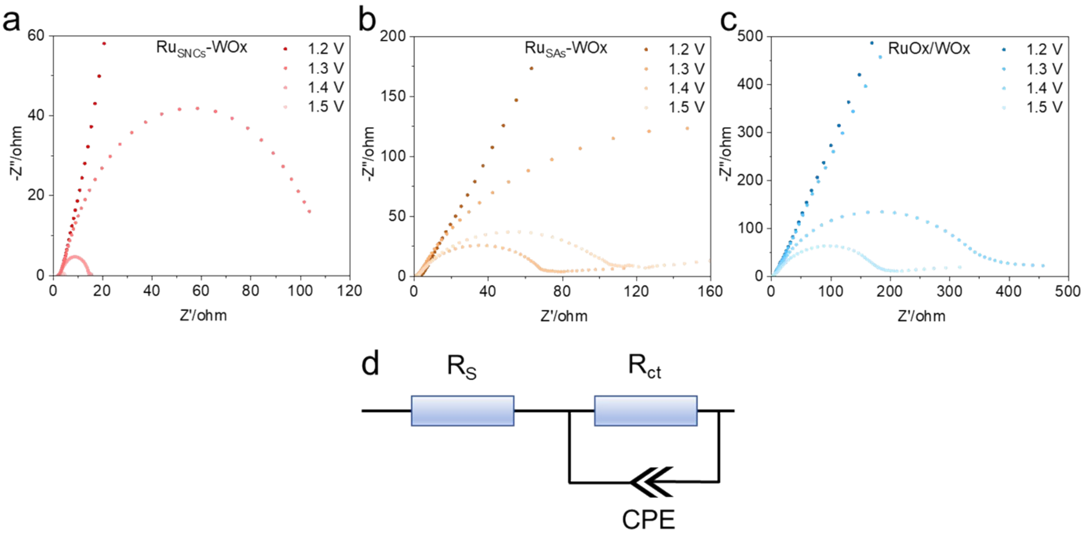

Fig. S25 Nyquist plots of (a) Ru_{SNCs}-WO_x; (b) Ru_{SAs}-WO_x and (c) RuO_x/WO_x at different Voltages. (d) Equivalent circuit used for fitting the Nyquist curves.

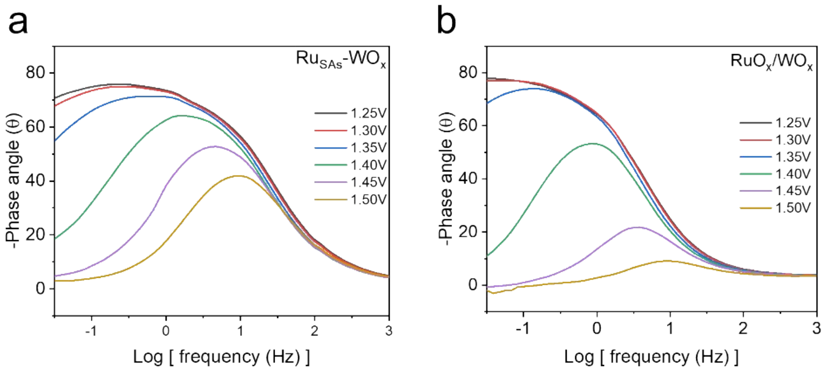

Fig. S26 Bode phase plots of (a) Ru_{SAs}-WO_x; (b) RuO_x/WO_x at different voltages.

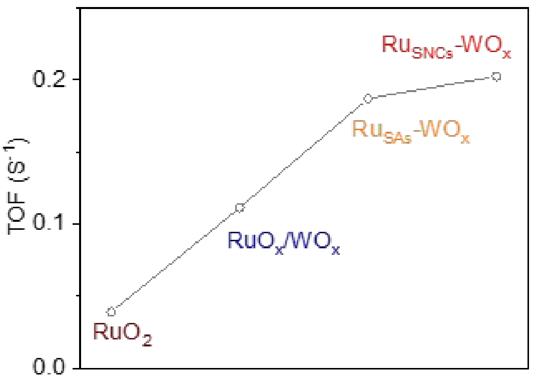

Fig. S27 TOF values of RuO$_2$, Ru$_{SNCs}$-WO$_x$, Ru$_{SAs}$-WO$_x$, and RuO$_x$/WO$_x$ at 1.55 V vs. RHE.

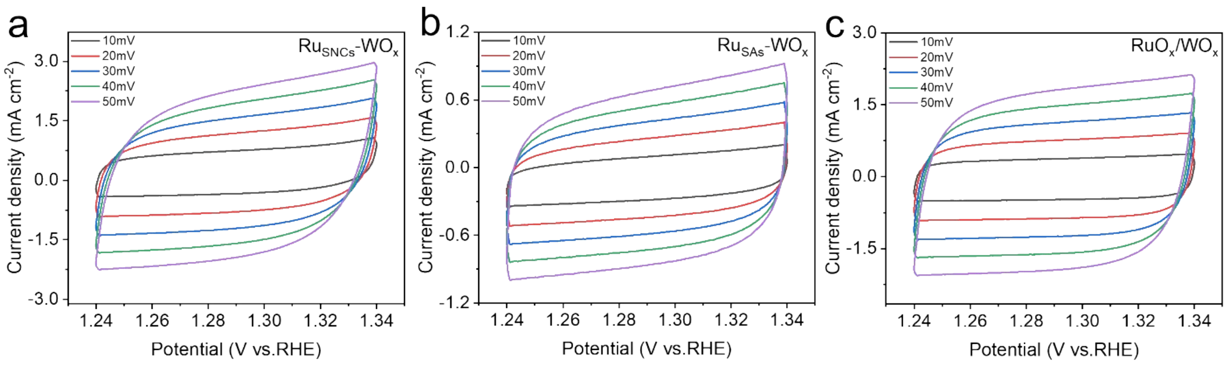

Fig. S28 CV curves of (a) Ru$_{SNCs}$-WO$_x$; (b) Ru$_{SAs}$-WO$_x$; (c) RuO$_x$/WO$_x$.

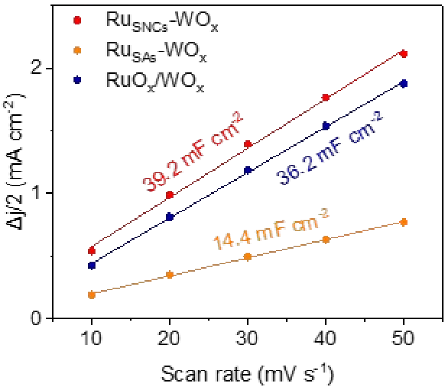

Fig. S29 The C$_{dl}$ values of Ru$_{SNCs}$-WO$_x$, Ru$_{SAs}$-WO$_x$, and RuO$_x$/WO$_x$ at different scan rates.

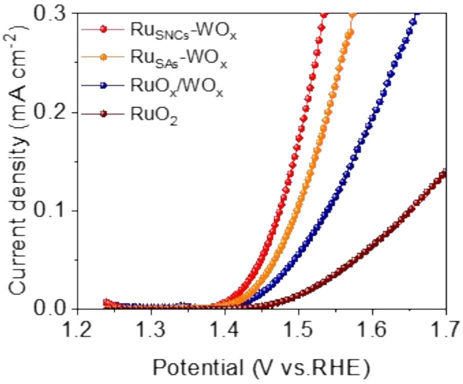

Fig. S30 OER polarization curves normalized by the ECSA for RuO_2, Ru_{SNCs}-WO_x, Ru_{SAs}-WO_x, and RuO_x/WO_x.

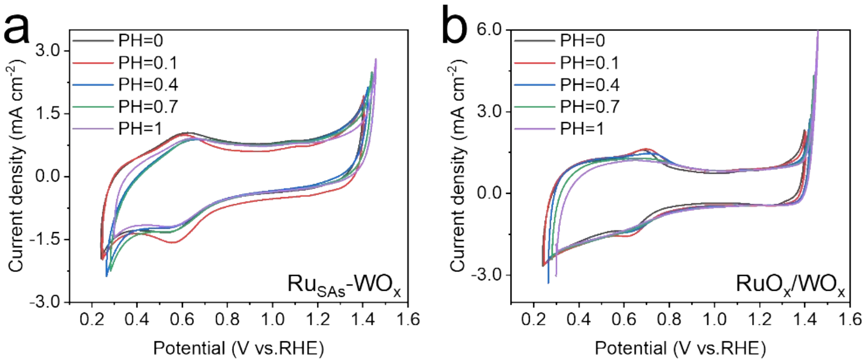

Fig. S31 pH independent CV analysis of redox peak of Ru_{SAs}-WO_x and RuO_x/WO_x measured from 0.0 to 1.4 V vs. SCE.

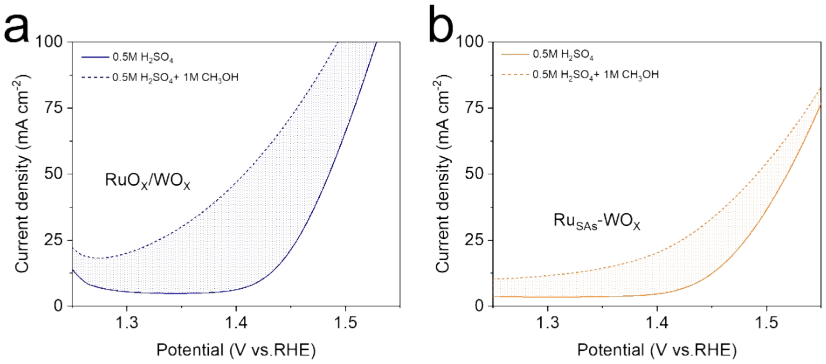

Fig. S32 LSV curves of (a) Ru_{SAs}-$WO_{x;}$ (b) RuO_x/WO_x recorded with and without 1 M methanol.

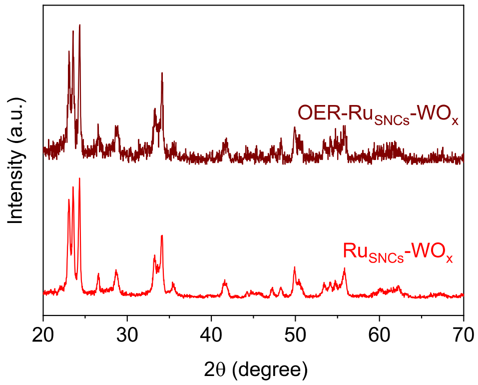

Fig. S33 XRD pattern of Ru$_{SNCs}$-WO$_x$ before and after OER stability test in 0.5 M H_2SO_4 solution.

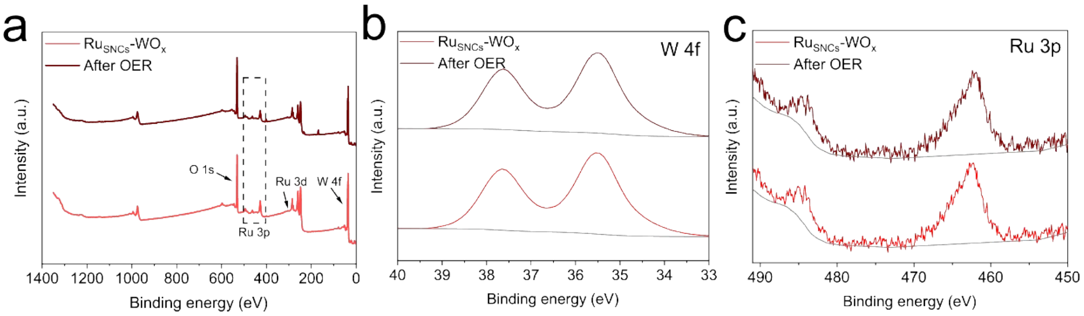

Fig. S34 XPS spectra of Ru$_{SNCs}$-WO$_x$ before and after OER stability test in 0.5 M H_2SO_4 solution.

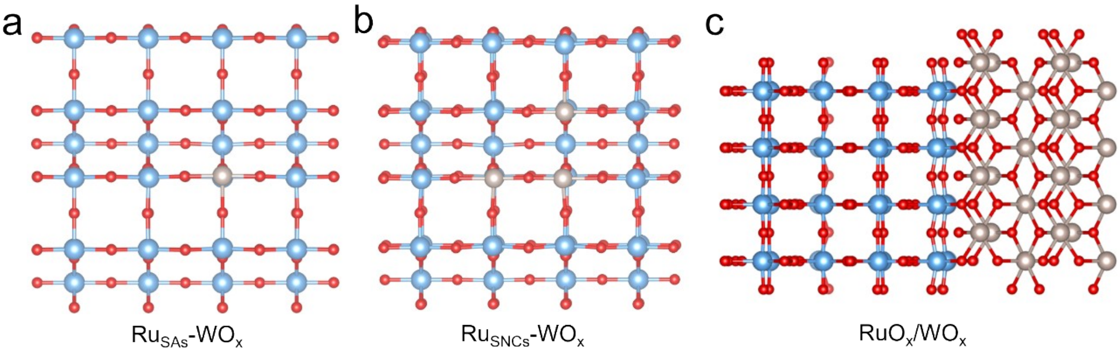

Fig.S35 The geometric configurations of (a) Ru$_{SNCs}$-WO$_x$; (b) Ru$_{SAs}$-WO$_x$; (c) RuO$_x$/WO$_x$.

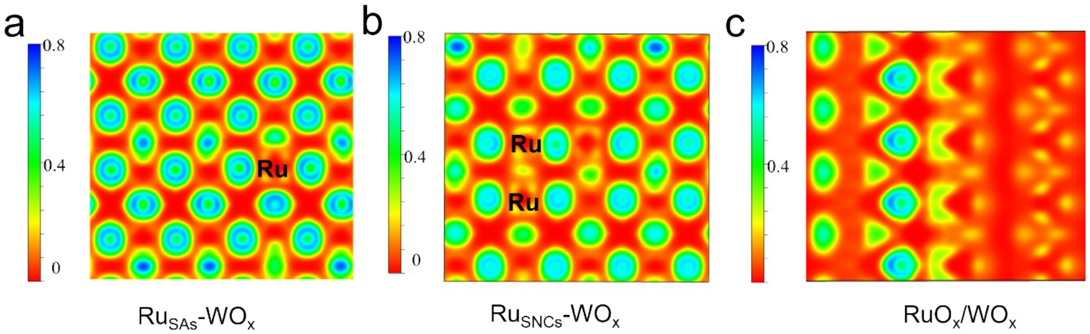

Fig. S36 The ELF graph for Ru_{SAs}-WO_x; Ru_{SNCs}-WO_x, and RuO_x/WO_x.

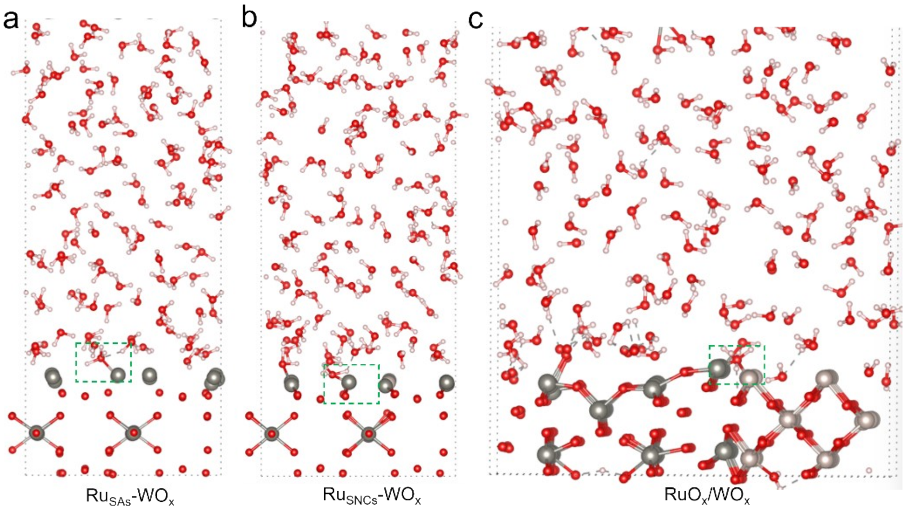

Fig. S37 Explicit solvation geometric configuration of (a) Ru_{SNCs}-WO_x; (b) Ru_{SAs}-WO_x; (c) RuO_x/WO_x.

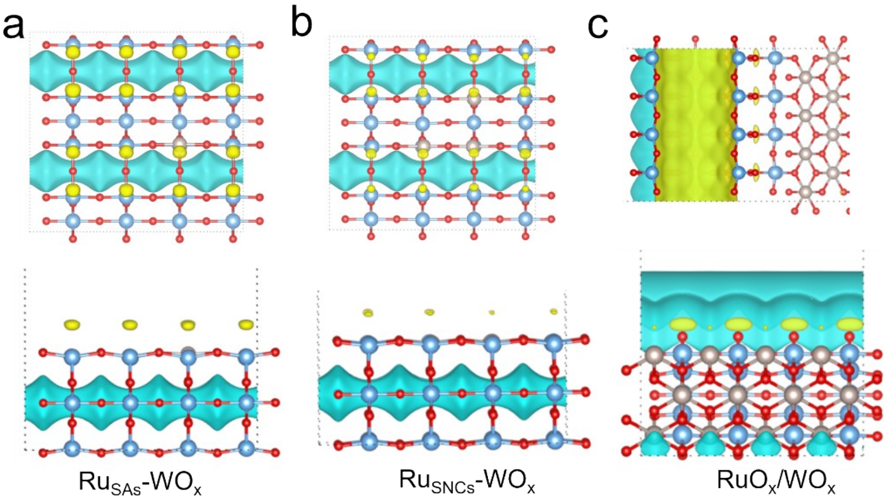

Fig. S38 Implicit solvation geometric configuration of (a) Ru_{SNCs}-WO_x; (b) Ru_{SAs}-WO_x; (c) RuO_x/WO_x.

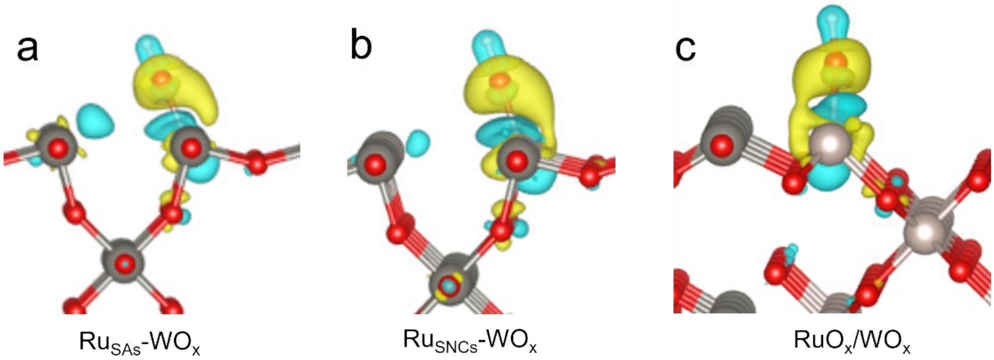

Fig. S39 Differential charge density for (a) Ru$_{SNCs}$-WO$_x$; (b) Ru$_{SAs}$-WO$_x$; (c) RuO$_x$/WO$_x$.

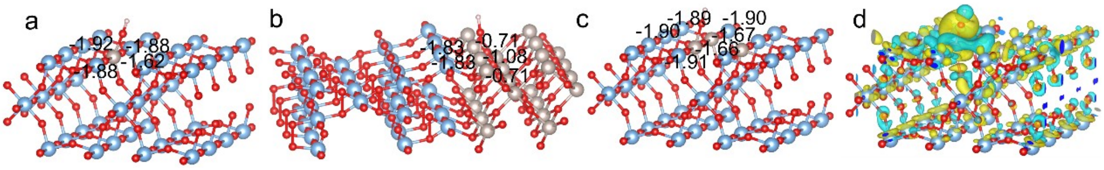

Fig. S40 Bader charge transfer of *OH adsorption: (a) Ru$_{SAs}$-WO$_x$, (b) RuO$_x$/WO$_x$, (c) Ru$_{SNCs}$-WO$_x$.. Difference Charge of *OH adsorption on (d) Ru$_{SNCs}$-WO$_x$.

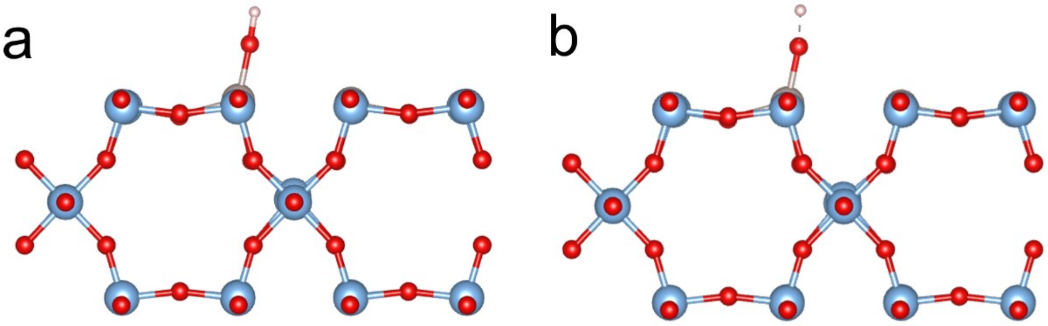

Fig. S41 The electron delocalization effect enhances the polarization of the adsorbed intermediate *OH on Ru$_{SNCs}$-WO$_x$.(a) Unpolarized(b) Polarized.

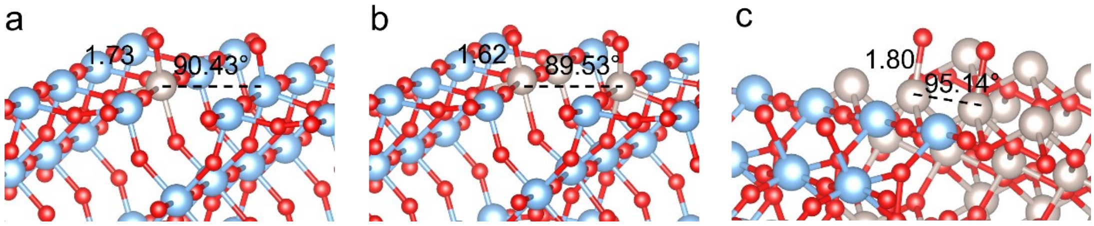

Fig. S42 The bond angle and bond length of the O*–Ru–*O moiety on the surface of (a) Ru$_{SNCs}$-WO$_x$; (b) Ru$_{SAs}$-WO$_x$; (c) RuO$_x$/WO$_x$.

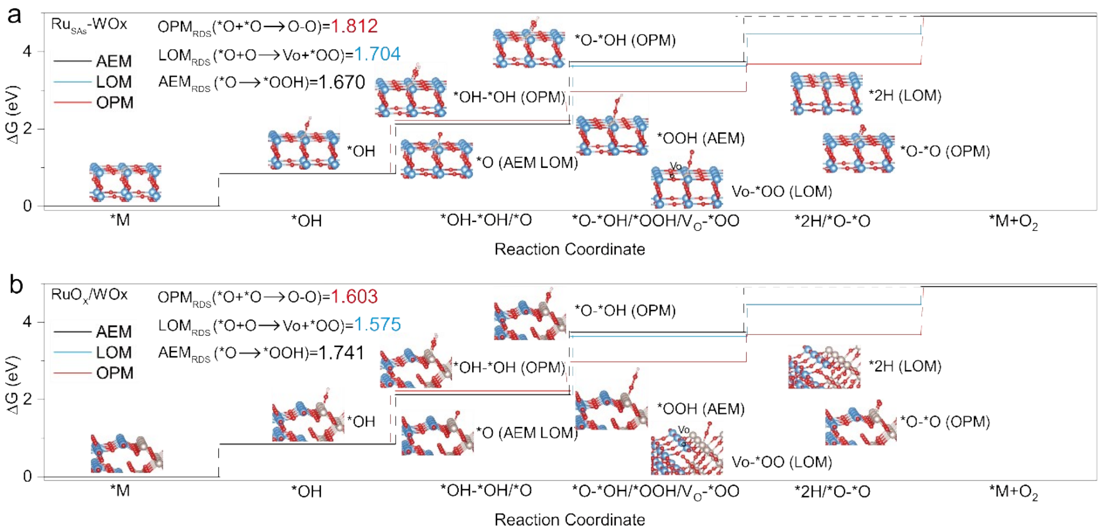

Fig. S43 The Gibbs free energy illustration by (a) Ru_{SAs}-WO_x, (b) RuO_x/WO_x atalysts during the OER process by AEM, LOM and OPM pathways.

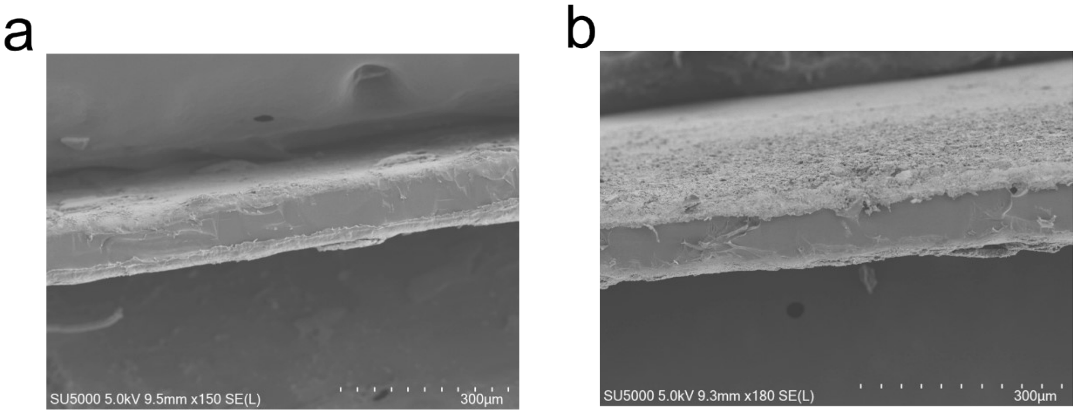

Fig. S44 The distribution of the catalyst on the membrane surface before (a) and after (b) the stability test.

Table S1 Structural parameters extracted from the Ru K-edge EXAFS fitting. (S_0^2=0.69).

Catalysts	shell	CN	R(Å)	σ^2	ΔE_0	R factor
Ru foil	Ru-Ru	12	2.672	0.00338	4.176	0.021
RuO_2	Ru-O_1	6	1.991	-0.00042	1.941	0.018
	Ru-Ru	6	3.153	0.00717		
	Ru-Ru_2	2	3.562	-0.00200		
Ru_{SAs}-WO_X	Ru-O_1	3.67	2.039	0.00440	-3.205	0.035
Ru_{SNCs}-WO_X	Ru-O_1	4.84	2.041	0.00398	-3.628	0.015
RuO_X/WO_X	Ru-O_1	5.58	2.016	0.00403	-1.254	0.031

Table S2. Comparison of representative Ru-based OER catalysts in 0.5 M H_2SO_4 electrolyte.

Catalyst	*j* (mA cm^{-2})	η (mV)	Stability	Reference
Ru_{SNCs}-WO_x	10	171	1000 h	This work
(Ru–W)Ox	10	170	300 h	1
Vn-RuO2	10	227	1050 h	2
$Ru_5W_1O_x$	10	227	550 h	3
RuO_2-CeO_2-CC	10	180	1000 h	4
ZnRuOx	10	230	320 h	5
Ru@V-RuO_2/C	10	176	25 h	6
Zn-RuO_2	10	173	1000 h	7
$Ru_{(anc)}$-Co_3O_4	10	198.5	150 h	8
$Ru_{0.1}Mn_{0.9}O_x$	10	210	1200 h	9
Zn-RuO2@ZnO	10	170	600 h	10
Ru–$Co_2MnO_{4.5}$	10	176	600 h	11

Table S3. PEMWE performance comparison of different catalysts..

Catalyst	Cell voltage (Vcell) @ 1 A cm^{-2}	Reference
Ru_{SAs}-WO_x	1.696	This work
Ni-RuO_2	1.95	12
Er-RuO_x	1.84	13
$H_{3.8}Ir_{1-x}Ru_xO_4$	1.78	14
RuFe@CF	1.898	15
PtRu-Co3O4	1.83	16
Ru/Ti_4O_7	1.78	17
M-$RuIrFeCoNiO_2$	1.85	18
Ru/TiO_x	1.71	19
Cr0.2Ru0.8O2-x	1.77	20

References

(1) L. Deng, S.-F. Hung, Z.-Y. Lin, Y. Zhang, C. Zhang, Y. Hao, S. Liu, C.-H. Kuo, H.-Y. Chen, J. Peng, J. Wang and S. Peng, *Adv. Mater.,* 2023, **35**, 2305939.

(2) Q. Qin, Z. Li, X. Zhao, H. Zhao, L. Zhai, M. G. Kim, J. Cho, H. Jang, S. Liu and X. Liu, *Angew.*

Chem. Int. Ed, 2024, **137**, e202413657.

(3) Y. Wen, C. Liu, R. Huang, H. Zhang, X. Li, F. P. G. d. Arquer, Z. Liu, Y. Li and B. Zhang, *Nat. Commun.,* 2022, **13**, 4871.

(4) H. Song, X. Yong, G. I. N. Waterhouse, J. Yu, H. Wang, J. Cai, Z. Tang, B. Yang, J. Chang and S. Lu, *ACS Catal.,* 2024, **14**, 3298-3307.

(5) P. Sun, Z. Qiao, X. Dong, R. Jiang, Z.-T. Hu, J. Yun and D. Cao, *J. Am. Chem. Soc.,* 2024, **146**, 15515-15524.

(6) Y. Li, W. Wang, M. Cheng, Y. Feng, X. Han, Q. Qian, Y. Zhu and G. Zhang, *Adv. Mater.,* 2023, **35**, 2206351.

(7) D. Zhang, M. Li, X. Yong, H. Song, G. I. N. Waterhouse, Y. Yi, B. Xue, D. Zhang, B. Liu and S. Lu, *Nat. Commun.,* 2023, **14**, 2517.

(8) Y. Hao, S.-F. Hung, W.-J. Zeng, Y. Wang, C. Zhang, C.-H. Kuo, L. Wang, S. Zhao, Y. Zhang, H.-Y. Chen and S. Peng, *J. Am. Chem. Soc.,* 2023, **145**, 23659-23669.

(9) J. Xu, C.-C. Kao, H. Shen, H. Liu, Y. Zheng and S.-Z. Qiao, *Angew. Chem. Int. Ed,* 2024, **69**, e202420615.

(10) Y. Qin, S. Deng, X.-Y. Zhou, Z. Yan, L. He, K. Li and T.-Y. Zhang, *J. Am. Chem. Soc.,* 2025, **147**, 30943–30955.

(11) M. Cai, G. Cai, K. Liu, D. Wang, H. Zhao and P. He, *J. Am. Chem. Soc.,* 2025, **147** 39953–39963.

(12) Z.-Y. Wu, F.-Y. Chen, B. Li, S.-W. Yu, Y. Z. Finfrock, D. M. Meira, Q.-Q. Yan, P. Zhu, M.-X. Chen, T.-W. Song, Z. Yin, H.-W. Liang, S. Zhang, G. Wang and H. Wang, *Nat. Mater.,* 2022, **22**, 100–108.

(13) L. Li, G. Zhang, C. Zhou, F. Lv, Y. Tan, Y. Han, H. Luo, D. Wang, Y. Liu, C. Shang, L. Zeng, Q. Huang, R. Zeng, N. Ye, M. Luo and S. Guo, *Nat. Commun.,* 2024, **15**, 4974.

(14) J. Tang, X. Liu, X. Xiong, Q. Zeng, Y. Ji, C. Liu, J. Li, H. Zeng, Y. Dai, X. Zhang, C. Li, H. Peng, Q. Jiang, T. Zheng, C.-W. Pao and C. Xia, *Adv. Mater.,* 2024, **36**, 2407394.

(15) J. Chen, Y. Ma, T. Huang, T. Jiang, S. Park, J. Xu, X. Wang, Q. Peng, S. Liu, G. Wang and W. Chen, *Adv. Mater.,* 2024, **36**, 2312369.

(16) D. Li, D. Xu, Y. Pei, Q. Zhang, Y. Lu and B. Zhang, *J. Am. Chem. Soc.,* 2024, **146**, 28728-28738.

(17) S. Zhao, S.-F. Hung, L. Deng, W.-J. Zeng, T. Xiao, S. Li, C.-H. Kuo, H.-Y. Chen, F. Hu and S. Peng, *Nat. Commun.,* 2024, **15**, 2728.

(18) C. Hu, K. Yue, J. Han, X. Liu, L. Liu, Q. Liu, Q. Kong, C.-W. Pao, Z. Hu, K. Suenaga, D. Su, Q. Zhang, X. Wang, Y. Tan and X. Huang, *Sci. Adv.,* 2023, **9**, adf9144.

(19) L. Zhou, Y. Shao, F. Yin, J. Li, F. Kang and R. Lv, *Nat. Commun.,* 2023, **14**, 7644.

(20) Y. Shen, X.-L. Zhang, M.-R. Qu, J. Ma, S. Zhu, Y.-L. Min, M.-R. Gao and S.-H. Yu, *Nat. Commun.,* 2024, **15**, 7861.